2016

Characteristics of flash initiations in a supercell cluster with tornadoes

Dong Zheng
State Key Laboratory of Severe Weather, Chinese Academy of Meteorological Sciences, NO. 46 Zhongguancun South Street, Beijing 100081, China, zhd@cams.cma.gov.cn

Donald R. MacGorman
Cooperative Institute for Mesoscale Meteorological Studies, University of Oklahoma and NOAA/OAR/National Severe Storms Laboratory

Atmospheric Research 167 (2016) 249–264

Contents lists available at ScienceDirect

Atmospheric Research

journal homepage: www.elsevier.com/locate/atmos

Characteristics of flash initiations in a supercell cluster with tornadoes

Dong Zheng [a,b,*], Donald R. MacGorman [c]

[a] State Key Laboratory of Severe Weather, Chinese Academy of Meteorological Sciences, NO. 46 Zhongguancun South Street, Beijing 100081, China
[b] Laboratory of Lightning Physics and Protection Engineering, Chinese Academy of Meteorological Sciences, Beijing 100081, China
[c] Cooperative Institute for Mesoscale Meteorological Studies, University of Oklahoma and NOAA/OAR/National Severe Storms Laboratory, Norman, OK, USA

ARTICLE INFO

Article history:
Received 29 May 2015
Received in revised form 22 July 2015
Accepted 23 August 2015
Available online 29 August 2015

Editor: J.L. Sanchez

Keywords:
Flash initiation
Supercell
Hydrometeor species
Tornado

ABSTRACT

Flash initiations within a supercell cluster during 10–11 May 2010 in Oklahoma were investigated based on observations from the Oklahoma Lightning Mapping Array and the Norman, Oklahoma, polarimetric radar (KOUN). The flash initiations at positions dominated by graupel, dry snow, small hail and crystals accounted for 44.3%, 44.1%, 8.0% and 3.0% of the total flashes, respectively. During the tornadic stage of the southern supercell in the cluster, flash initiations associated with graupel occupied the main body, the right flank and the forward flank of the supercell, while those associated with dry snow dominated the outskirts of the adjacent forward anvil, right anvil and rear anvil. The flash initiations associated with small hail were concentrated around the main updraft, particularly toward its front side. Highly dense flash initiations were located in the regions overlying the differential reflectivity (Z_{DR}) arc and right anvil. The average initial height of the flashes decreased gradually from the rear to the front and from the right to the left flanks, while the height range over which initiations occurred reached a maximum at the front of the updraft. The flashes that were initiated in the adjacent forward anvils were largest on average, followed by those in the regions ahead of the updraft and near the Z_{DR} arc. This study supports the concept of charge pockets and further deduces that the pockets in the right anvil are the most abundant and compact due to the frequent flash initiations, small-sized flashes and thin layers including flash initiations.

1. Introduction

Flash initiation is a basic scientific issue in the field of atmospheric electricity (Dwyer and Uman, 2014). One flash is thought to initiate at a point with a large electric-field magnitude (which usually lies between positive and negative charges) and propagates with two opposite-polarity leaders: the negative leader enters the positive charge and the positive leader enters the negative charge (Mazur, 1989a, 1989b; Shao and Krehbiel, 1996; Coleman et al., 2003). The charge structure, which greatly impacts flash initiation, is related to the microphysics and kinematic structure of the storm. Storms with strong updrafts, which may transport water vapor into higher regions in clouds (in favor of ice-phase processes), experience more frequent collisions among ice particles and charge transfers (Takahashi, 1978; Saunders and Peck, 1998; Berdeklis and List, 2001; Saunders et al., 2006) and bring adjacent charge regions closer together (MacGorman et al., 1989) to produce higher density of flash initiations (i.e., flash rates) than normal storms (e.g., Wiens et al., 2005; Tessendorf et al., 2007; Calhoun et al., 2013).

Some previous studies reported distributions of flash initiations with altitude. For example, Proctor (1991) found that the distribution of the origin heights of 773 flashes within 13 thunderstorms was bimodal, with peaks at 5.3 km and 9.2 km above mean sea level. Lund et al. (2009) reported that flashes were mainly initiated within two altitude ranges (3–6 and 7–10 km MSL) in a small mesoscale convective system (MCS) with a normal tripolar charge structure. Payne et al. (2010) suggested that flash initiations were more frequent at 7 km than at lower levels in their analysis of a supercell storm. In a high-precipitation supercell storm, Calhoun et al. (2013) observed that flash initiations reached a maximum near 10–11 km during the early–middle stage and bi-level maxima during the middle-posterior stage of a storm's life. The observed single-level or double-level distributions of flash initiations should be connected with the dipolar or tripolar dominant charge structures in thunderstorms.

The studies also related the initial positions of flashes to the structures of thunderstorms. Proctor (1991) documented that 66% of 658 flashes began within approximately 270 m of the 20-dBZ contours; 27% of flashes were initiated inside these contours (most of these began at the edges of high-reflectivity cores); and the remaining 7% began outside the 20-dBZ contour. Similar results (73%, 19% and 8%) were obtained for 276 high-level flashes that began above 7.4 km, but 195 CG flashes scored 54%, 36% and 9% and showed a greater tendency to begin inside the 20-dBZ contours. In an investigation of two cells in a small MCS, Lund et al. (2009) revealed that most flashes were initiated within the 35 dBZ contours of convective cells embedded within a

* Corresponding author at: Tel: +86 10 58995148, fax: +86 10 68408941.
E-mail address: zhd@cams.cma.gov.cn (D. Zheng).

http://dx.doi.org/10.1016/j.atmosres.2015.08.015
0169-8095/

convective line. Payne et al. (2010) noted that the initiation points at 7 km mainly corresponded to low differential reflectivity (Z_{DR}) and weak updrafts (<10 m s^{-1}) during the pre-tornado stage and dissipating stage of a supercell storm. However, the initiation points at 7 km were distributed in a more extensive range during the mature stage with tornadoes, particularly toward the southern and eastern sides of the reflectivity hook, with the eastern parts in strong updraft regions (>15 m s^{-1}). In contrast, Calhoun et al. (2013) revealed that areas with many flash initiations were in and near updrafts ≥20 m s^{-1} but usually outside regions with updrafts ≥40 m s^{-1}.

On the other hand, many observations have indicated that flashes are mainly initiated in or near the cores of storms (e.g., Wiens et al., 2005; Tessendorf et al., 2007). Recent studies provided information on flash initiations in distant anvils. Kuhlman et al. (2009) first presented observations of flashes initiated in anvils several tens of kilometers from the convective core of a storm. The authors suggested that in situ charging was responsible for the large electric field that initiates flashes. Weiss et al. (2012) also reported flashes that were initiated in the forward anvil in several supercells whose initial positions corresponded to the local reflectivity maximum, the region between the main charge and the screening layer, and intersecting anvils from two adjacent storms. The authors related the flash initiations in the anvils to embedded convection.

With its special capability in identifying the hydrometeor species, polarimetric radar data have been combined with the flash activity of thunderstorms recently, which significantly deepened the understanding of the relationship between microphysical process and electric process (e.g., Dotzek et al., 2001; Bruning et al., 2007; Lund et al., 2009; Payne et al., 2010). In this study, radar data from the Norman, Oklahoma, polarimetric radar (KOUN) and flash data from Oklahoma Lightning Mapping Array (OK-LMA) were combined to investigate the association of the flash initiations and the structures of a supercell cluster. Supercells have been widely researched in terms of flash activity. Extremely frequent intra-cloud (IC) flashes, low proportions of cloud-to-ground (CG) flashes (e.g., MacGorman et al., 1989, 2005; Wiens et al., 2005; Tessendorf et al., 2007), changes in the dominant polarity of CG flashes with types of supercells (high precipitation or low precipitation, e.g., Branick and Doswell, 1992; Knupp et al., 2003), complex charge structures (e.g., Stolzenburg et al., 1998; MacGorman et al., 2005; Wiens et al., 2005; Bruning et al., 2010), and lightning holes (e.g., Krehbiel et al., 2000; Goodman and Coauthors, 2005; Payne et al., 2010) have been studied. However, only limited studies specifically considered the characteristics of initiation points of flashes (e.g., Payne et al., 2010; Calhoun et al., 2013; mentioned above). In this study, we focus on the topical subject to the following questions: what are the features of flash initiations in density, height, height range and size of their leading flashes in a supercell storm and what are the relationships of these features to the hydrometeors and dynamic structures of a supercell storm?

2. Instrumentation and data processing

2.1. Oklahoma Lightning Mapping Array (OK-LMA)

OK-LMA, which includes 10 stations (Fig. 1), locates the breakdown of flashes at a very high frequency (VHF, 60 − 66 MHz). Details of the technology, accuracy, and operation can be found in Rison et al. (1999), Krehbiel et al. (2000), Thomas et al. (2004) and MacGorman and Coauthors (2008).

Following previous work (e.g., Lund et al., 2009), only the sources located by at least 7 stations with a chi-square goodness-of-fit value $\chi_v^2 \leq 2$ (Thomas et al., 2004) were chosen for this study. The algorithm for reconstructing an individual flash from sources was introduced by MacGorman and Coauthors (2008). However, the original algorithm was found to perform poorly when the storms were vigorous and where sources were highly concentrated, with a large number of flashes

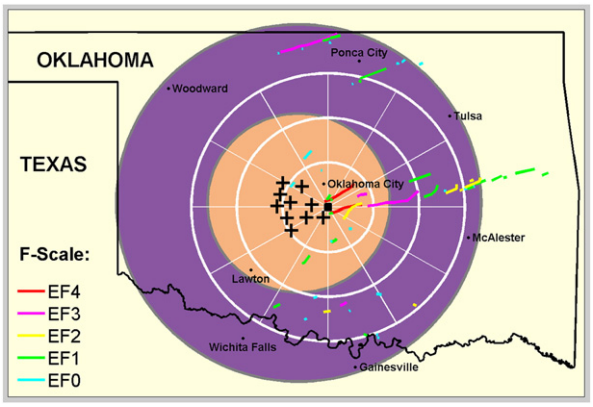

Fig. 1. Map showing the coverage of the Oklahoma Lightning Mapping Array (OK-LMA) and the KOUN polarimetric radar, along with tracks of tornadoes during 10–11 May 2010 (UTC). The positions of the OK-LMA stations are shown by "+" symbols. The red-orange shading (within 100 km of the center of OK-LMA) indicates the area in which lightning can be mapped in three dimensions. The purple shading (100–200 km from the center of OK-LMA) indicates the area in which two-dimensional locations of sources are reliable. The white circles show distances of 50, 100, and 150 km from the KOUN radar. The color key for the EF scale ratings given to the tornadoes as rated by the National Weather Service is shown in the lower left. The cluster of supercells analyzed in this study was mainly located to the area within 100 km of the centers of the OK-LMA and the KOUN radars.

having the duration of 3 s which is the longest duration permitted by the algorithm. Therefore, new combinations of thresholds were tested while retaining the original algorithm and the permitted flash duration (3 s). The flashes identified by each combination of thresholds were compared with manual analyses to identify the best combination. Based on these tests, a potential flash source must occur within 180 ms of the previous source and within 2 km and 300 ms of any other flash source; these thresholds differ from those used in the original formulation (MacGorman and Coauthors, 2008), i.e., 150 ms, 3 km and 500 ms, respectively. Flashes with 10 or fewer points were not used. The algorithm described by Lund et al. (2009) was used to determine the initial position of a flash, which was calculated as the centroid of a compact cluster of the initial 10 points; the influence of outliers has been removed.

The flash size is expressed by using the area of the convex hull of the horizontal plan projection of VHF source points that belong to the same flash. A convex hull, which is the polygon produced by allowing a band to contract on all the points constituting the flash (Fig. 2), was used by Bruning and MacGorman (2013) to calculate the minimum area that collects all the source points of one flash in their study on flash-size spectra. This area showed a good flash-size metric in describing the 2-D extension of one flash.

2.2. National Lightning Detection Network (NLDN)

Data from the National Lightning Detection Network (NLDN; Orville, 2008) were used to describe the CG flash activity of the supercells. To exclude NLDN data that might incorrectly identify an IC flash as a CG flash (e.g., Cummins et al., 1998; Johnson and Mansell, 2006), only positive cloud-to-ground (PCG) flashes with peak currents greater than 15 kA and negative cloud-to-ground (NCG) flashes with peak currents less than −15 kA were extracted. These thresholds were chosen based on experience analyzing thunderstorms, particularly supercells with inverted charge structures (such as the supercells studied here).

2.3. KOUN polarimetric radar

The KOUN polarimetric radar is located in Norman, Oklahoma (Fig. 1). In addition to the traditional variables of reflectivity factor at horizontal polarization Z_{HH}, velocity, and spectrum width, this S-band radar provides additional polarimetric variables, including differential reflectivity (Z_{DR}), copolar cross-correlation coefficient (ρ_{hv}), and

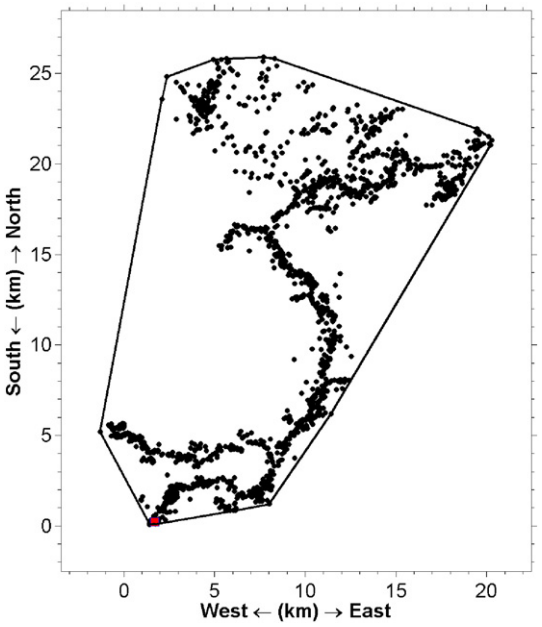

Fig. 2. Example of the horizontal projection of VHF source points belonging to a flash at 2223:20 UTC 10 May 2010. The distances are relative to the KOUN radar position. The convex hull is defined by the solid line with an area of 346 km^2. The red square marks the initial position of the flash.

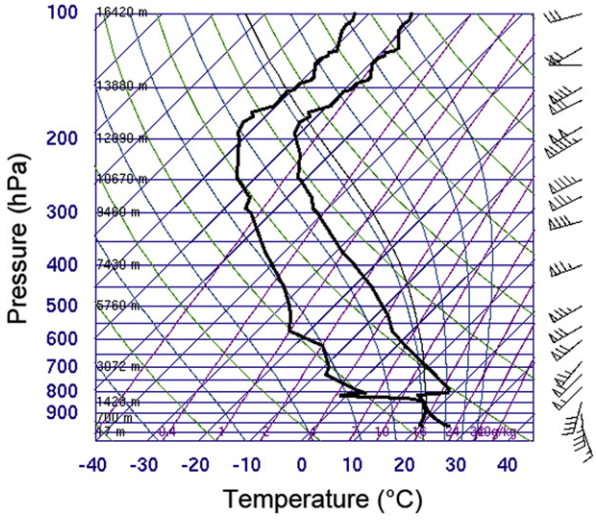

Fig. 3. Skew-*T*/log-*P* diagram of the temperature and dewpoint temperature from the 2100 UTC sounding at the Norman, Oklahoma on 10 May 2010, provided by the National Weather Service (NWS) Forecast Office. The original skew-*T*/log-*P* diagram was provided by the University of Wyoming and downloaded from http://weather.uwyo.edu/upperair/sounding.html. We cropped the image and added the axes labels.

differential phase shift (Φ_{DP}). The specific differential phase (K_{DP}) was computed from Φ_{DP}. The details on the dual-polarization variables were provided by Kumjian (2013a, b, and c). Studies on the polarimetric characteristics of supercells can be found in Dotzek et al. (2001), Loney et al. (2002), Kumjian and Ryzhkov (2008), Van Den Broeke et al. (2008), Snyder et al. (2010, 2013), Palmer et al. (2011), among others.

In this study, the hydrometeor classification algorithm (HCA) developed by Park et al. (2009) was used to classify hydrometeors. The HCA includes the quality control of the polarimetric variables. This method classifies 10 types of radar echoes: 1) ground clutter, including that due to anomalous propagation (GC/AP); 2) biological scatterers (BS); 3) dry aggregated snow (DS); 4) wet snow (WS); 5) crystals of various orientations (CR); 6) graupel (GR); 7) "big drops" (BD); 8) light and moderate rain (RA); 9) heavy rain (HR); and 10) a mixture of rain and hail (RH, written as rain/hail hereafter). In addition, the radar time used in the following text refers to the time when one volume scan starts at the first tilt (0.5°).

3. Overview of the supercell cluster

3.1. Evolution of the storms

A tornado outbreak with a total of 55 documented tornadoes from 13 storms occurred in Oklahoma (Fig. 1) from 10 May to 11 May 2010 (UTC; afternoon and evening of 10 May 2010, CDT). More information on this outbreak can be found in Palmer et al. (2011). The environment in which the storms developed was characterized by strong low-level shear, high convective available potential energy (CAPE) (2759 J kg^{-1} at Norman, Oklahoma, at 2100UTC), as shown in Fig. 3.

The composite reflectivity of the analyzed cluster of supercells observed by the KOUN radar is shown in Fig. 4. Over its lifetime, the storm cluster experienced merging of storms in the south and splitting in the north during its move from west by south to east by north. Storm initiation within the cluster occurred at approximately 2051:52 UTC. As they developed, by 2109:09 UTC, three separate storms were present to the west-southwest of the KOUN radar, as shown in Fig. 4a. By 2126:24 UTC (Fig. 4b), these three storms were in the process of merging (the 30-dBZ contours at low levels still separated from each other), which were located to the west of the KOUN radar (between $y = -30$ km and $y = 30$ km, where y is the distance north of the KOUN radar). By 2146:50 UTC (Fig. 4c), an EF0 tornado had developed within the supercell of the cluster. Two new storms occurred to the southwest of the cluster. The northern one, however, did not develop further and seemed to be quickly absorbed into the cluster. The southern one developed rapidly and later became a supercell. By 2212:40 UTC (Fig. 4d), the storm just south of the KOUN radar was strengthening. Meanwhile, two storms located to the north of the line $y = 60$ km were splitting from the cluster. By 2234:09 UTC (Fig. 4e), the southern storm had merged into the cluster, while a storm straddling the $y = 60$ km line was splitting away from the cluster. Three tornadoes occurred in the supercells during this period. The analysis ended at 2258:51 UTC (Fig. 4f) when the main body of the cluster moved out of the region of reliable analysis (see Fig. 1). At that time, another storm located at $y = -20$ km and $x = 50$ km was merging into the cluster. After that, the cluster produced an EF3 tornado in its southern region which is not considered here.

Because separating one storm from another is difficult, the storms in the cluster were studied as a whole. In addition, the cluster is referred to as a supercell cluster because the storms ultimately developed into supercell storms.

3.2. Overall height and frequency of flash initiations

Fig. 5 shows the LMA sources in the supercell cluster starting at 2058 UTC and the CG flashes starting from 2122 UTC. The flash frequency continued to increase after 2240 UTC, while the source frequency decreased; this finding is partly due to the decrease in the detection efficiency of OK-LMA at large distances.

Fig. 5a indicates that the sources were first observed at heights of 5–12 km (MSL, same to below) and were then extended from the surface to 15 km. During the early stage (2110 − 2130 UTC), the region with the highest density of sources occurred at a height of approximately 9 km; this height decreased to 6 km between 2130 UTC and 2145 UTC and subsequently rose to approximately 8 km at 2200 UTC; then, the heights varied between 7 and 9 km. Although the initial heights of the flashes were widely distributed (mainly between 6 and 12 km), the level with the greatest initial positions (the red solid line in Fig. 5a) was always above the level with the largest number of sources (the black solid line in Fig. 5a); the levels were approximately 2 km apart after 2150 UTC.

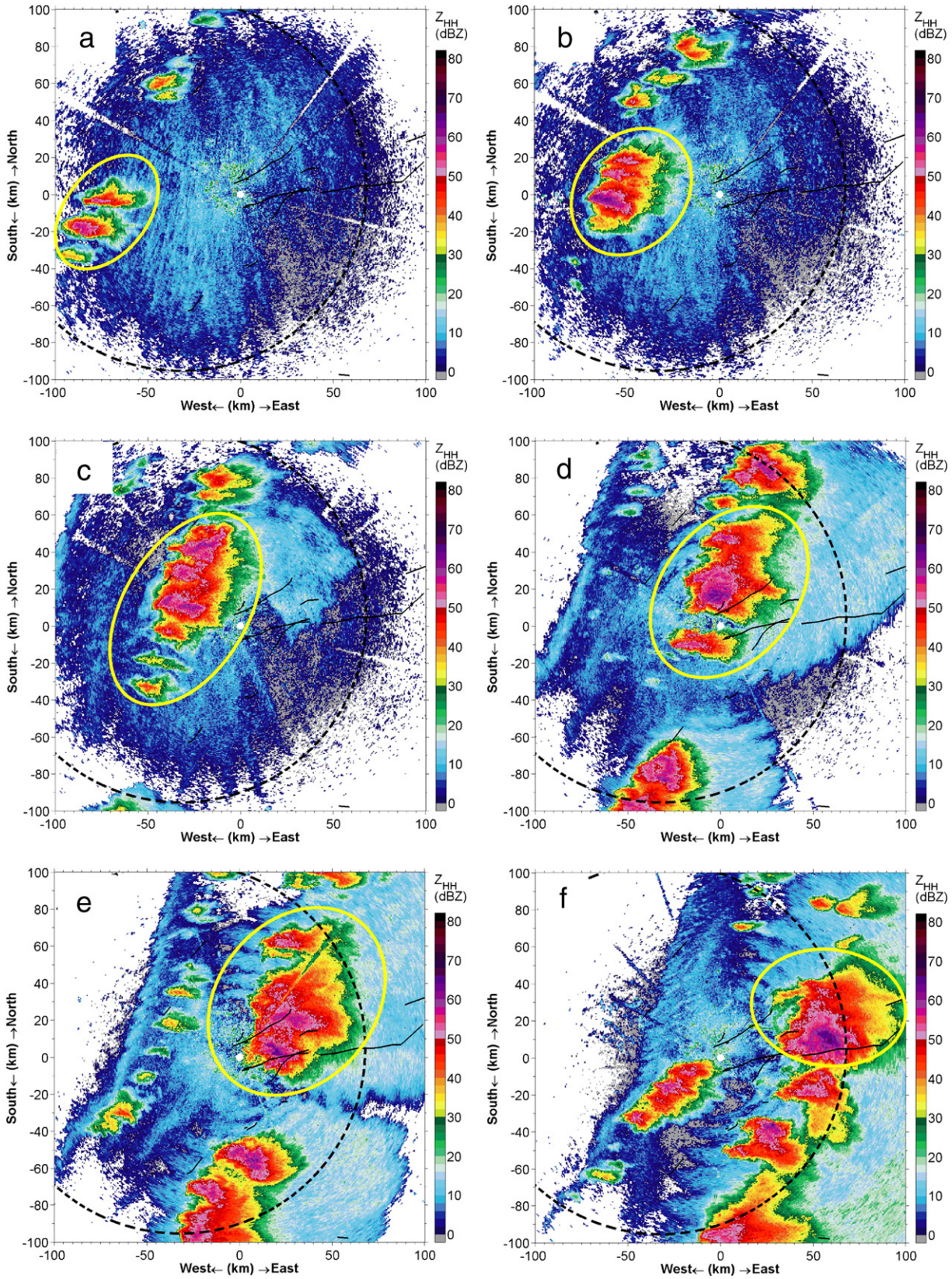

Fig. 4. Evolution of the cluster of supercells shown by the composite reflectivity of the KOUN radar. (a) 2109:09 UTC; (b) 2126:24 UTC; (c) 2146:50 UTC; (d) 2212:40 UTC; (e) 2234:09 UTC; and (f) 2258:51 UTC. The dashed circle encloses the region within 100 km of the center of OK-LMA. The solid yellow ellipses encircle the main bodies of the analyzed cluster. The tracks of tornadoes are shown as black solid lines. Distances (km) are shown to the east (*x*-axis) and north (*y*-axis) of the KOUN radar.

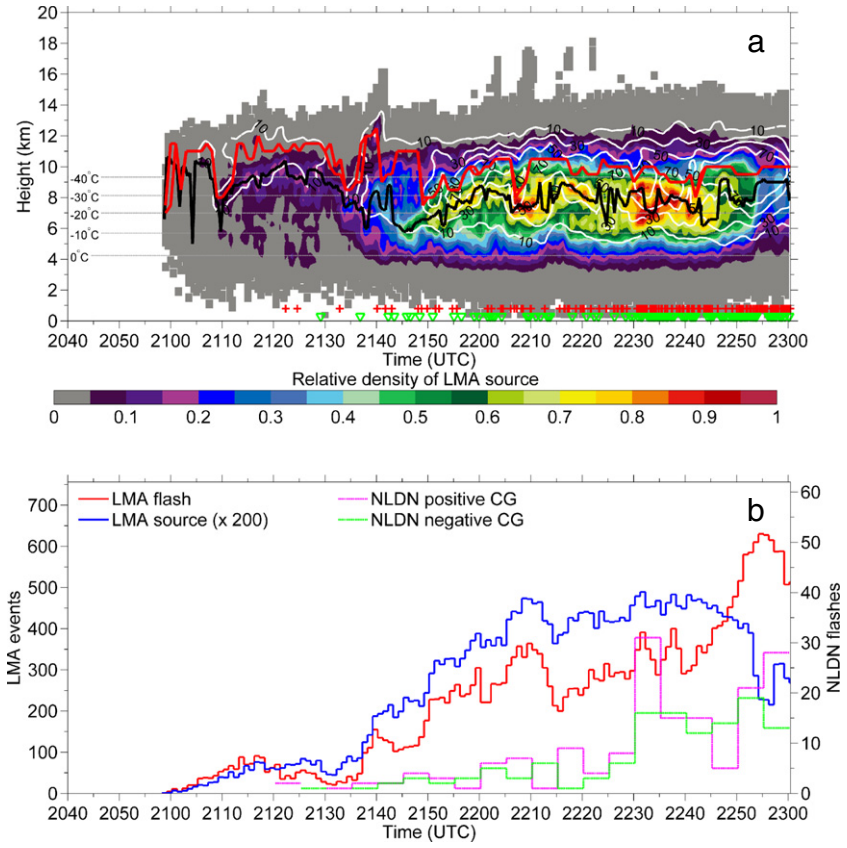

Fig. 5. Overall lightning activity in the supercell cluster. (a) Density of sources as a function of height and time; the colors indicate the relative density (0.5-min interval and 0.2-km span), and the white contour lines indicate the density of the initial positions of the lightning as a function of height and time (1-min interval and 0.5-km span). The black and red solid lines mark the heights with the maximum source density and the heights with the most initiation points, respectively. The positive (red "+") and negative (green "∇") CG lightning times are marked near the time axis. Levels with environmental temperatures of 0 °C, −10 °C, −20 °C, −30 °C and −40 °C are plotted as gray dashed lines. (b) Average number of lightning flashes and sources observed in 1-min intervals by OK-LMA and positive and negative CG lightning flashes observed by the NLDN in 5-min intervals.

The LMA data were used to infer the charge regions that participated in the discharges according to the method introduced by previous authors (Rust and Coauthors, 2005; Wiens et al., 2005; Bruning et al., 2007, 2010; MacGorman and Coauthors, 2008; Li et al., 2013), which is based on the concept that a flash leader traverses charged regions of opposite polarity (Shao and Krehbiel, 1996; Coleman et al., 2003) and the observations that sources associated with negative breakdown of flash radiate greater power (Shao and Krehbiel, 1996; Rison et al., 1999; Thomas et al., 2001). Therefore, the main positive charge regions that participated in the discharge were expected to be located at the middle levels, which indicated an overall inverted electric structure (Rust and Coauthors, 2005; Tessendorf et al., 2007; Bruning et al., 2014) in the main body of the cluster.

The lightning activity (Fig. 5b) was extreme, with a total of 27,297 flashes recorded by the OK-LMA during the analysis period. However, only 291 NLDN CG flashes were recorded, an extremely low proportion of the total (1.07%). Meanwhile, the proportion of PCG flashes to the CG flashes reached 56.70%, which is much higher than climatological values (approximately 6%−10% in the analysis region; see Fig. 9 in Orville and Huffines, 2001). Numerous in-cloud flashes, low ratios of CG flashes, and high ratios of PCG flashes were also reported in other severe storms and were attributed to broad and strong updrafts (e.g., MacGorman et al., 1989; Lang et al., 2000; Soula et al., 2004).

3.3. Flash initiations and associated hydrometeors

Flashes that initiated 2 min before and 2 min after the central time of a volume scan and within 100 km of the center of OK-LMA were selected for this general analysis, and initiations in the cone of silence of radar were removed from the dataset. The hydrometeors at the initial positions of the flashes were provided by the HCA. A total of 17,344 samples were ultimately chosen for the statistical analysis.

During the evolution of the cluster in the analysis period, the initial positions of the flashes were dominated by four types of hydrometeors (Fig. 6a): graupel, dry snow, rain/hail and crystals, accounting for 44.3%, 44.1%, 8.0% and 3.0% of the total samples, respectively. Within the analysis window, 99.4% of the flash initiations were associated with these four types of dominant hydrometeors. In addition, during most periods, more than 85% of the flash initiations were associated with graupel and dry snow.

Fig. 6b indicates that the first dominant hydrometeor associated with the flash initiations changed with height. The proportion corresponding to graupel increased from 4 km to a maximum (64.9%) at 7 km, where the temperature was approximately −20 °C; then, the proportion of flashes decreased to a minimum at 11 km. The proportion of the flash initiations associated with dry snow began to increase at 4 km and terminated at 11 km, where the maximum was 74.8%. The proportion of the flash initiations associated with crystals increased above 5 km to a maximum of 13.7% at 13 km.

The hydrometeor classification algorithm does not distinguish the proportion of rain and hail in a mixture. It was necessary to assess if the hail was in a wet environment (hail with water coat or surrounded by rain) or in a dry environment (dry surface and less surrounding rain) for the flash initiations associated with the classification of rain/hail. Therefore, the data associated with the rain/hail classification were plotted on the axes of Z_{HH}−Z_{DR}, Z_{HH}−ρ_{hv}, and Z_{HH}−K_{DP} (Fig. 7a−c). In

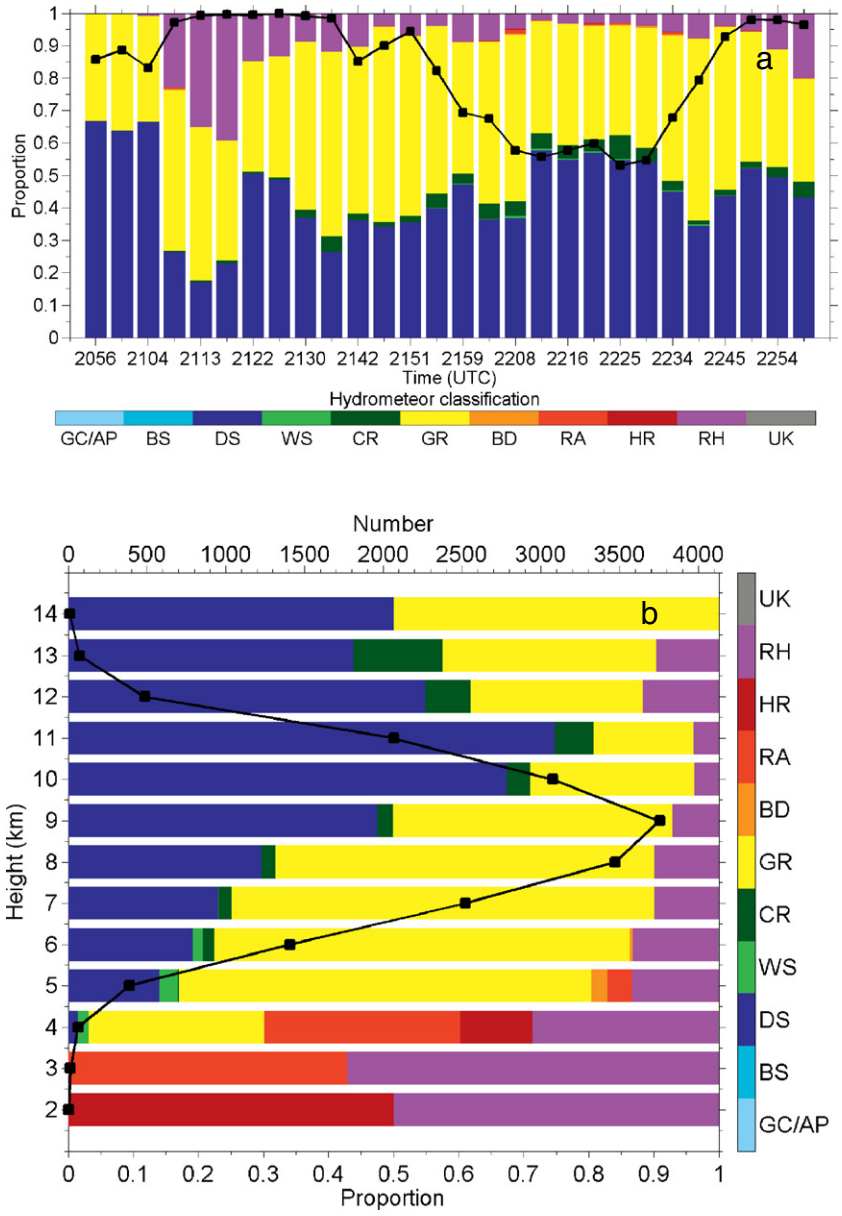

Fig. 6. The distribution of flash initiations associated with special dominant hydrometeors. (a) Distribution by volume scan time. The black solid line depicts the ratio of the available initiation points to the total set, distinguishing the impact of the radar's cone of silence. (b) Distribution of heights. The black solid line depicts the variation in the number (top *x* axis) of initiation points with height.

Fig. 7, the hydrometeor regions defined by Straka et al. (2000) were superposed (Fig. 7a–c), and the height distribution of the flash initiations associated with this classification was added (Fig. 7d).

The ratios of the samples above 0 °C, −10 °C, −20 °C, −30 °C, and −40 °C to the total samples were approximately 98.7%, 92.5%, 72.5%, 46.5% and 21.3%, respectively. Fig. 7a–c reveals that the majority of the samples were narrowly distributed. The overwhelming majority had Z_{HH} values from 40 to 60 dBZ, Z_{DR} values from −1 dB to 0.3 dB, ρ_{hv} values from 0.95 to 1, and K_{DP} values from −0.5 deg km^{-1} to 0.5 deg km^{-1}. These ranges of the polarimetric variables indicate that most of the initiations were located at positions dominated by high concentrations of small hail with a dry surface or in an environment with less rain: 1) a large ρ_{hv} should not be caused by a mixture of hail and rain, which would reduce the value of ρ_{hv} to less than 0.95 (Balakrishnan and Zrnić, 1990; Straka et al., 2000); 2) large hail also tends to cause a small ρ_{hv} at least on account of resonance effects (Balakrishnan and Zrnić, 1990; Kumjian et al., 2013a,2013b,2013c); and 3) the existence of rain or melting shells would contribute to large Z_{DR} and K_{DP} (Ryzhkov et al., 2013).

4. Flash initiations in supercells during the tornadic stage

The relationships of the flash initiations to the structures of supercells with tornadoes are discussed in this section. Four volume scans starting at 2234:09 UTC and ending at 2250:14 UTC were chosen for the following reasons: 1) the structure of the cluster that could be detected by the KOUN radar was relatively integrated and the main bodies of the cluster were meanwhile located within 100 km of the center of OK-LMA; and 2) the southern supercell in the cluster exhibited a usual supercell structure, which made it possible for us to relate the characteristics of flash initiations to the typical structure of supercell (ref. Lemon and Doswell, 1979; Markowski, 2008; Wang et al., 2010; Davies-Jones, 2015; Manzato et al., 2015).

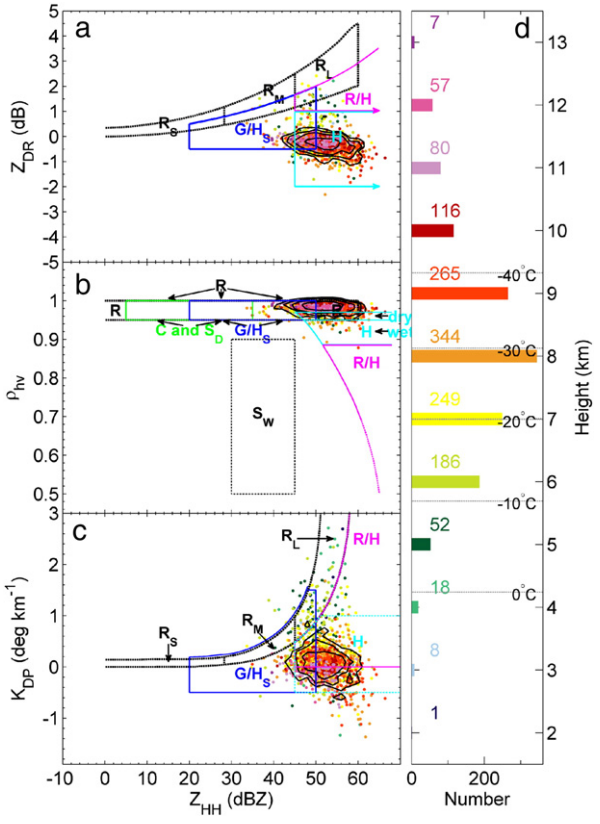

Fig. 7. Scattergrams of polarimetric parameters at the positions of flash initiation points associated with the classification of rain/hail for (a) Z_{HH}–Z_{DR}, (b) Z_{HH}–ρ_{hv}, (c) Z_{HH}–K_{DP} and (d) distribution of the initial flash positions with height. The delineated regions of hydrometeors were adopted from Straka et al. (2000, Fig. 2, Fig. 3 and Fig. 4). The black contour lines depict the number of points within each grid cell at (a) 2 dBZ − 0.2 dBZ, (b) 2 dBZ − 0.01, and (c) 2 dBZ − 0.1 deg km^{-1}. The contour values are 5, 10, 20, and 50 when moving toward the center. G/H$_S$: graupel/small hail; H: hail; R/H: rain/hail; R$_S$: small-size rain; R$_M$: medium-size rain; R$_L$: large-size rain; C: ice crystals; S$_D$: dry snow; and S$_W$: wet snow. The colors used for the points in (a), (b), and (c) represent heights, as shown in (d).

Fig. 8 exhibits the sector scans of Z_{HH} and Z_{DR} of the cluster at 0.9° tilt during the analysis period. At 2234:09 UTC, the southern supercell had nearly completely merged with the northern supercell in one scan time. The northern supercell produced an EF4 tornado, while the southern supercell yielded another EF4 tornado (Fig. 8a1 and a2). The southern supercell further strengthened at 2238:27 UTC with a clear hook echo (southwest of the main body). The southern supercell was producing two tornadoes simultaneously at this time (~2245 UTC) while the tornado associated with the northern supercell was still ongoing. So, there were actually three tornadoes in progress at the time presented in Fig. 8c1–c2. At 2250:14 UTC (Fig. 8d1 and d2), the two tornadoes in the southern supercell nearly intersected, leading to a relatively large area with near-zero Z_{DR}. The tornado in the middle supercell was ongoing, while that in the northern supercell was dissipating.

The southern supercell is the focus of the analysis because of its classical structure including its hook echo, notches associated with inflow and main updrafts (UD), and Z_{DR} arc (south part of the main body). The Z_{DR} arc refers to the region along the gradient of Z_{HH} along the inflow side of the forward flank of supercell storms, where the value of Z_{DR} is usually greater than 3 dB at the low levels (Fig. 8a2, b2, c2, and d2). The size-sorting hypothesis, in which strongly veering wind shear in supercell environments advects raindrops from their source positions, was believed to result in a region of large drops along the southern edge of the forward flank downdraft (FFD) (e.g., Kumjian and Ryzhkov, 2008, 2009; Dawson et al., 2014).

A sketch of the low-level supercell structure given by Lemon and Doswell (1979), which was rotated to fit this case, was portrayed on a schematic diagram to describe the southern supercell in the cluster in Fig. 9. The directional terms used below are defined in the upper-left corner of Fig. 9. Note that anvil regions, which are identified by referring to the extension of the reflectivity at different heights, are depicted by red lines in Fig. 9. The region at the front of the main body of the supercell is defined as the adjacent forward anvil to distinguish from the forward anvils strictly defined by Kuhlman et al. (2009) and Weiss et al. (2012). These authors identified a flash as an anvil flash if it began or extended more than 30 km downshear of the 30-dBZ reflectivity contour around the main precipitation core of the storms at the mean anvil height. No flash was initiated in the region defined using these criteria during this volume scan. The right anvil mainly extended toward the south, while the rear anvil spread toward the west of the cluster. The extension of the rear anvil was small, with the boundary nearly overlapping the western edge of the 30-dBZ echo contour, which is likely due to the impact of the environmental wind at this high level.

4.1. Dominant hydrometeors associated with the flash initiations

The flash initiations, whose colors indicate specific hydrometeor species, are plotted on the 30-dBZ contour at 0.9° tilt in Fig. 10. By assessing the reflectivity at each 0.5-km level, the top positions of the bounded weak echo regions (BWERs) are marked by stars in the figures, except for Fig. 10a, in which the top position cannot be clearly distinguished because of the impact of the cone of silence of radar. At 2245:56 UTC and 2250:14 UTC, the BWERs were most distinguishable. Note that the entire BWER was tilted, and its top ascended from 5 to 7 km and inclined toward the front of the supercell.

Three types of dominant hydrometeors, i.e., graupel, dry snow, and small hail, were most distinctly associated with flash initiations; these hydrometeors showed clear regional differences. The flash initiations at the positions dominated by graupel were mainly distributed within the main body, right flank, and forward flank of the supercells. The flash initiations associated with dry snow were mainly located around the areas characterized by initiations in graupel-dominating regions, near the outskirts of the adjacent forward anvil, right anvil, rear anvil and northern margin of the cluster. The flash initiations at the positions where small hail dominated were aggregated in the regions near the main updrafts. In addition to the southern supercell, in which the region containing these small hail-associated initiations extended and inclined to the front of the updraft as the storm strengthened, the other supercells in the cluster also experienced small hail-associated initiations near or around their updrafts.

4.2. Density of the flash initiations

Fig. 11 displays the density of the initiation points of the flashes. At 2234:09 UTC and 2238:27 UTC, the densest flash initiations in the southern supercell occurred in the regions to the front of the updraft and along the areas overlying the Z_{DR} arc. In addition, the north zonal regions with active initiations in the northern supercell during the first two scans were also near the regions overlying the Z_{DR} arc. In these areas, the density of flash initiations reached 2–5 fl km^{-2} within 4 min (the following density values are all within 4 min). The region corresponding to the right anvil also experienced frequent flash initiations; the center had peak values of 6 fl km^{-2} at 2234:09 UTC and 3 fl km^{-2} at 2238:27 UTC. At 2245:56 UTC and 2250:14 UTC, as the middle supercell developed, the most frequent flashes occurred in the regions where the middle supercell and the northern supercell combined. During these two scans, as the southern supercell developed, the flash initiations in the regions overlying the Z_{DR} arc weakened, and the maximum densities were usually smaller than 2 fl km^{-2}. In comparison, the frequent flash initiations observed to the front of the region overlying the Z_{DR} arc and those corresponding to the eastern part of the right anvil increased, with a density of 2–4 fl km^{-2}. Meanwhile, the central and western parts of the right anvil maintained relatively

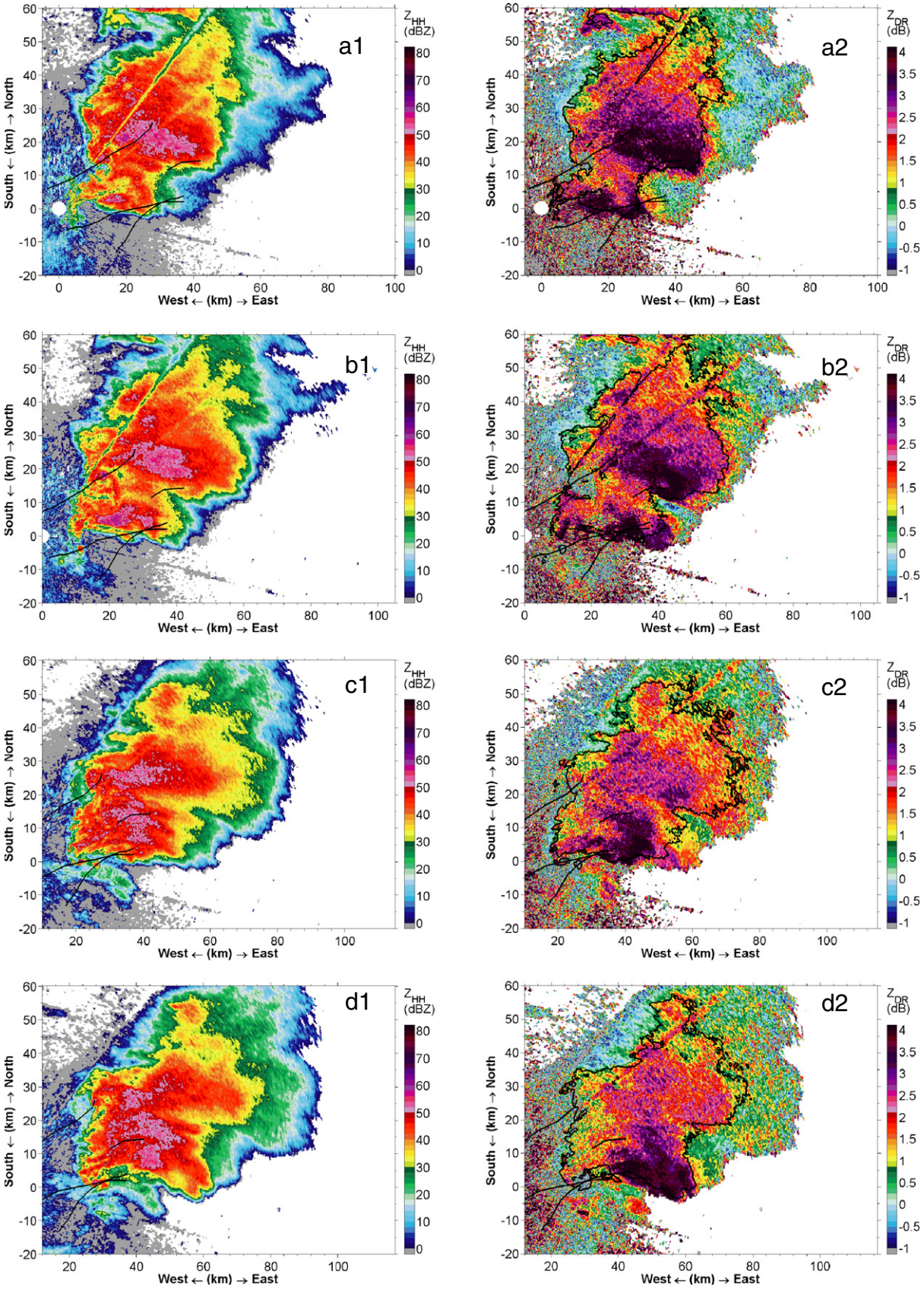

Fig. 8. KOUN radar measurements of Z_{HH} (left) and Z_{DR} (right) at 0.9° tilt at (a) 2234:09 UTC, (b) 2238:27 UTC, (c) 2245:56 UTC, and (d) 2250:14 UTC. The 30-dBZ contours of Z_{HH} are superposed on the Z_{DR} images.

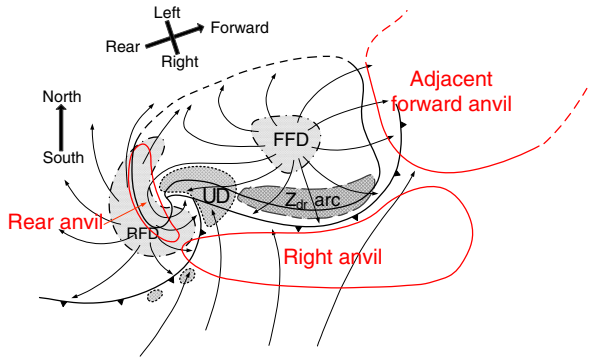

Fig. 9. Schematic of the southern supercell in the cluster. The basic structure of the supercell at low level was given by Lemon and Doswell (1979).The diagrams depicted by the black lines indicate the structures at low levels, and those depicted by the red lines indicate some of the structures at higher levels. The dotted line in the northern part of the contour around the main body indicates that no edge existed because the southern and northern supercells merged. The dotted lines and open gap in the region labeled "adjacent forward anvil" indicate the possible additional stretching of the anvil. UD: main updraft; FFD: forward flank downdraft; RFD: rear flank downdraft.

active flash initiations; some areas had densities greater than 2 fl km^{-2}, except at 2245:56 UTC. Note that a narrow area with few flash initiations (<0.5 fl km^{-2}) exists between the two regions with active initiations (the right anvil and the region overlying the Z_{DR} arc). Flash initiations in the rear of the southern supercell (and the northern supercells) were generally rare and weakly increased when the southern supercell developed. Low initiation density was observed in updraft regions, throughout the FFD, and through the adjacent forward anvil region.

4.3. Average height and height range of the flash initiations

The initiation points of the flashes generally undergo a step-by-step average height decrease from right to left and from the rear to the front in Fig. 12a1, b1, c1 and d1. In the right and rear peripheries, the initial positions were usually located above 10 km, which meant that these initiations were caused by the right and rear anvils. Great heights for the flash initiations were also observed in the region near the updraft, particularly to the west of the updraft. In contrast, the flash initiations in the regions to the front of the updraft tended to have an average height of 7–8 km. The regions approximately overlying the Z_{DR} arc were characterized by flash initiations at heights of 8–9 km, sometimes extending to the west or east. To the north of these regions, the heights of the initiations were approximately 7–8 km, although some locations had large values (>9 km) in some scans. The lowest-altitude flash initiations (4–5 km) could be found in the adjacent forward anvil, although some locations with relatively large heights were also interspersed. Because of the dependence of flash initiations on strong electric fields, the height distribution of the initial positions of the flashes might embody that of large electric fields.

Fig. 12a2, b2, c2 and d2 shows the height ranges of the initial positions of the flashes. The values were calculated by subtracting the minimum height from the maximum height in each horizontal grid. Focusing on the southern supercell, we found that the greatest height range lies in the region at the front of the main updraft, where strong entrainment may have occurred (Browning and Foote, 1976; Klemp and Wilhelmson, 1978; Nelson, 1983; Tessendorf et al., 2005). During the four scans, the height ranges were substantially greater than 2 km in these regions, even reaching 7 km at 2245:56 UTC. A relatively small region to the rear of the updraft had a height range larger than

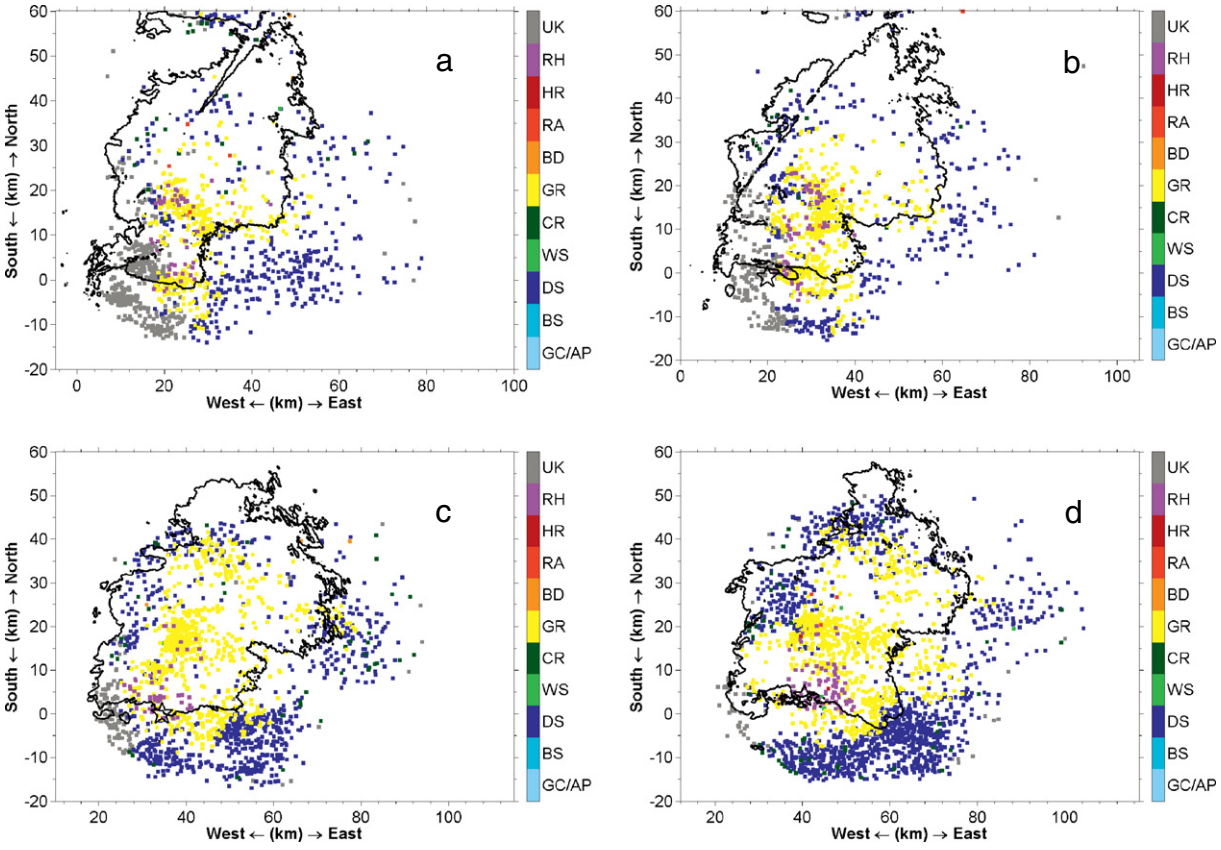

Fig. 10. Initiation points of flashes, which are colored according to their associated dominant hydrometeor superposed by the 30-dBZ contour at 0.9° tilt. (a) 2234:09 UTC; (b) 2238:27 UTC; (c) 2245:56 UTC; and (d) 2250:14 UTC. The gray color means that the hydrometeor is unknown or cannot be obtained because the initiation points were located in the radar's blind sector. The top positions of the bounded weak echo regions (BWERs) are marked by stars in the images, except for those at 2234:09 UTC, when the BWER could not be clearly distinguished because of the radar's blind sector.

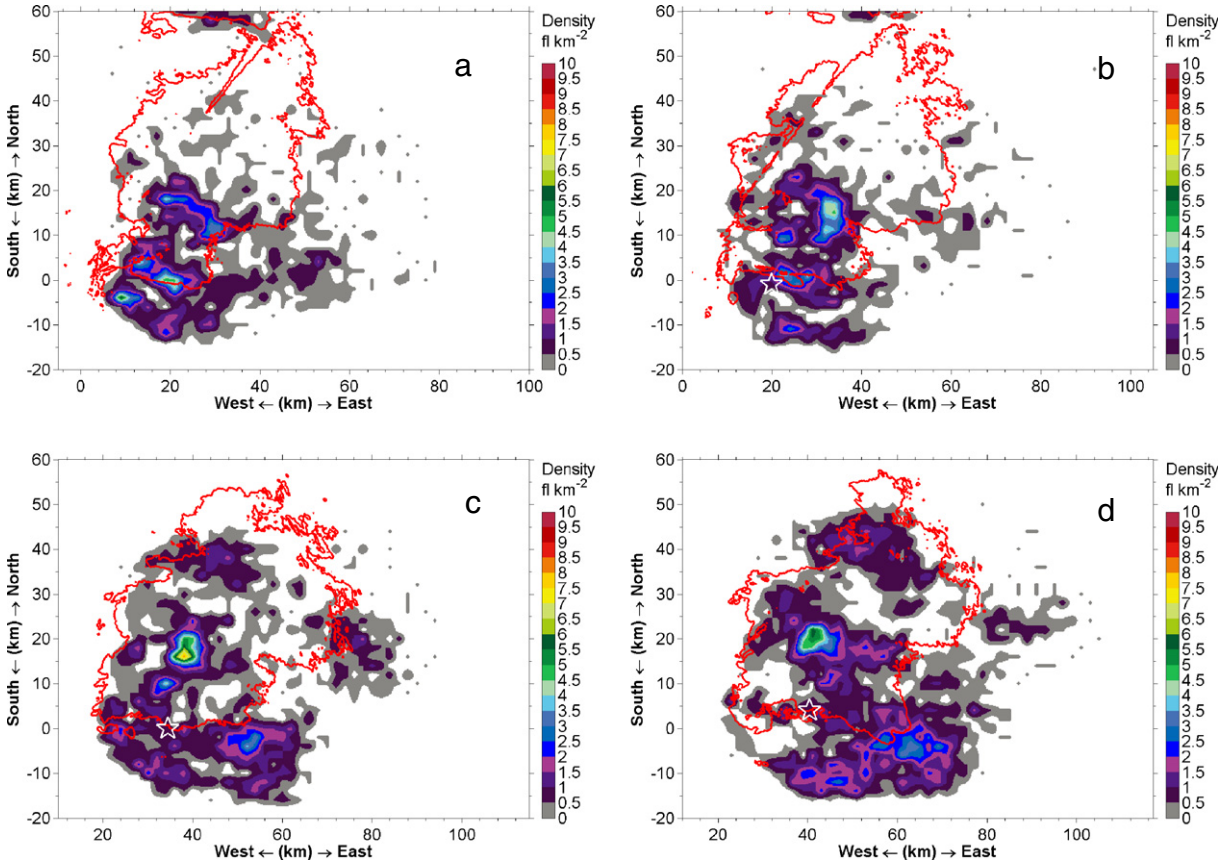

Fig. 11. Density of flash initiation points superposed by the 30-dBZ contour at 0.9° tilt. (a) 2234:09 UTC; (b) 2238:27 UTC; (c) 2245:56 UTC; and (d) 2250:14 UTC. The statistical grids are 2 km × 2 km. The data are shown after bilinear interpolation for better display. The same as in Figs. 12–13.

2 km. In the first two scans, the regions approximately overlying the Z_{DR} arc also had large height ranges (>2 km). As the supercell developed, the areas with large height ranges seemed to move into the eastern part of the right anvil, similar to the initiation density (see Fig. 11). Overall, the right and rear anvils were principally characterized by small height ranges (<2 km) and were interspersed by values larger than 2 km. The adjacent forward anvil featured similar height intervals for the initiations in the right anvil.

4.4. Area of the convex hull of the flashes led by the initiations

Fig. 13 illustrates where flashes with different average convex-hull areas were initiated. The flashes that were initiated in the adjacent forward anvils tended to be large; the average areas of the convex hulls of flashes larger than 100 km^2 accounted for a relatively high proportion of the total area. The relatively large flashes that originated in the regions near the southern edge of the 30-dBZ contour, particularly in the region ahead of the main updraft and near the region overlying the Z_{DR} arc, had average areas larger than 25 km^2. A region with relatively large flash initiations appeared near the intersection of the southern supercell and the adjacent supercell to its north. Comparatively, the flashes that originated in the rear and right anvils were usually small, with convex-hull areas under 25 km^2.

4.5. Conceptual models

To summarize the above results and to elucidate the critical conclusions, some schematics of conceptual models that describe the characteristics of flash initiations and their relationships to the structures of supercells are shown in Fig. 14. The southern supercell in the cluster is principally depicted. Based on the above results, the northern part of the supercell is not considered because its merging process may have been complex. The models display macroscopic characteristics, which might be more universal than neglected minor details. The situations during the vigorous stage (corresponding to the last two scans) are slightly preferable.

5. Discussion

Non-inductive charging (Takahashi, 1978; Saunders and Peck, 1998; Berdeklis and List, 2001; Saunders et al., 2006) is generally accepted as the primary charging process in thunderstorms. In this process, ice particles gain charge as they collide. Large and small particles are oppositely charged; the polarity is mainly affected by the temperature and liquid water content. Usually, graupel and ice crystals are considered to be the main particles with opposite polarity charges. With the action of the updraft, the particles with different weights separate in height, which leads to the different-polarity dominant charge levels within the storm. The flashes are usually initiated by the strong electric fields which are located between two regions with different-polarity charge. In this study, the flashes that primarily originated where graupel and dry snow (the aggregation of ice crystals) dominated accounted for approximately 88% of the total, which is consistent with the non-inductive charging mechanism. When studying multicell storms and a MCS, Bruning et al. (2007) and Lund et al. (2009), respectively, reported that flashes typically originated near the boundary between graupel and ice crystals, often within or near the graupel regions. In this study, the flash initiations within the main body of the supercell and its right and forward flanks were at positions where graupel dominated. However, the flash initiations in the rear and outskirts of the right and adjacent forward anvils were explicitly associated with dry snow. Therefore, a regional difference exists regarding the dominant hydrometeors

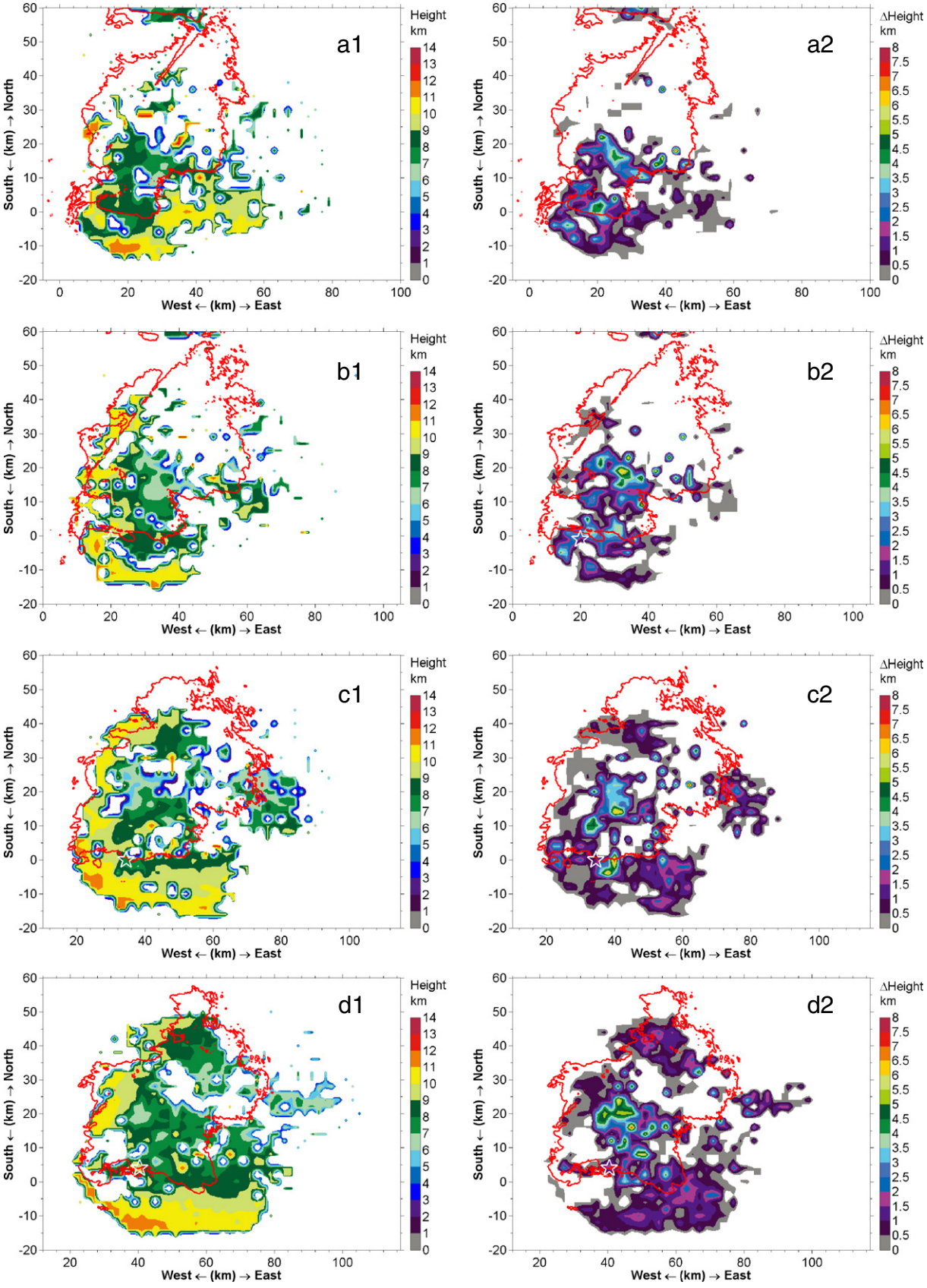

Fig. 12. Average height (left) and height range (right) of flash initiation points superposed by the 30-dBZ contour at 0.9° tilt. (a) 2234:09 UTC; (b) 2238:27 UTC; (c) 2245:56 UTC; and (d) 2250:14 UTC. The average height values that show large gradients along the edges between the grids with values and those without values are not reliable due to the interpolation.

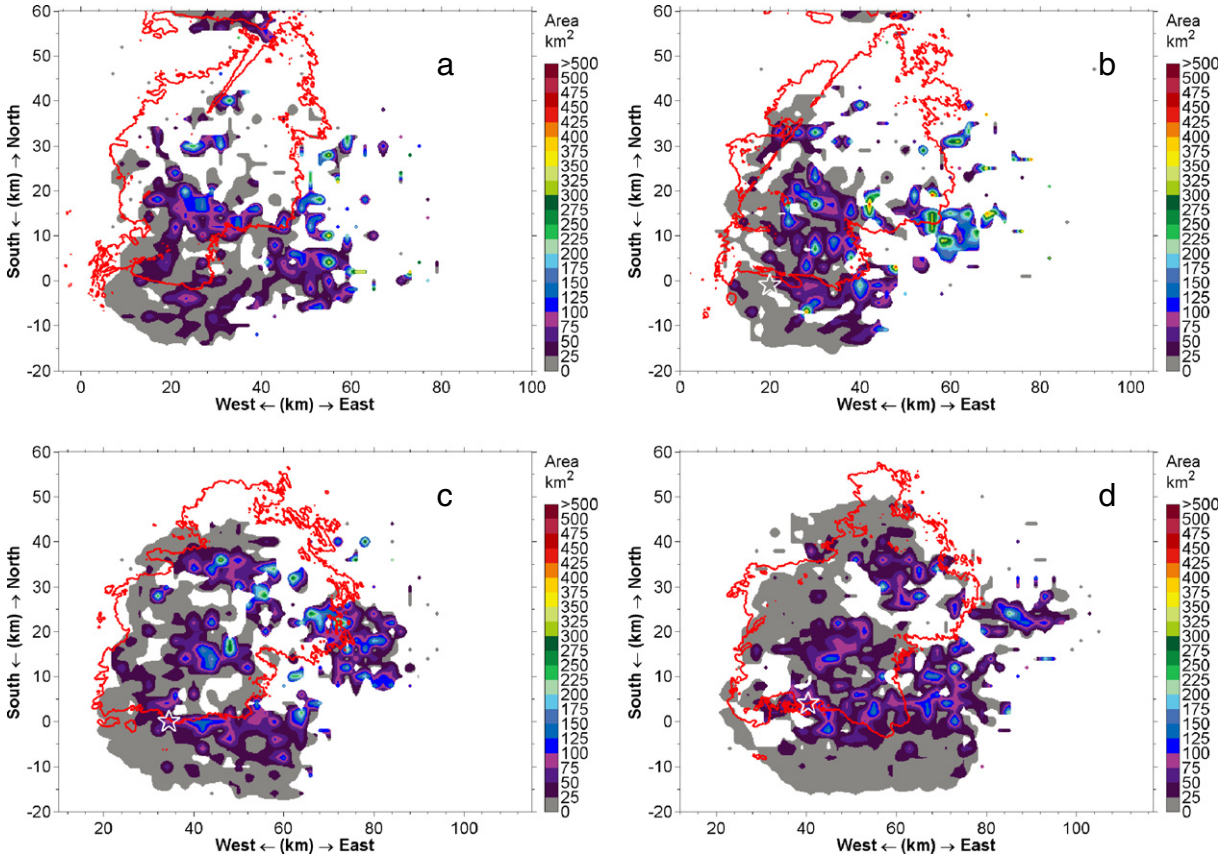

Fig. 13. Average area of the convex hull of the flashes shown at their initial positions superposed by the 30-dBZ contour at 0.9° tilt. (a) 2234:09 UTC; (b) 2238:27 UTC; (c) 2245:56 UTC; and (d) 2250:14 UTC. The average areas of the flashes are labeled at their initiation positions, which distinguish where the different-sized flashes originated.

associated with flash initiations in supercell storms, indicating that the strong electric fields that cause the initiations may not always lie between regions dominated by graupel and ice crystals.

Dynamic processes seemed to have a critical impact on the characteristics of flash initiations. Light, dry snow was transported far from the region around the updraft relative to heavy hail and graupel. The incline of the small-hail flash initiations toward the front of the updraft might be due to the strong recycling, entrainment, and repeat growth of hydrometeors on the forward flank of the updraft where strong cyclonic flow and shear exist (Browning and Foote, 1976; Klemp and Wilhelmson, 1978; Nelson, 1983; Tessendorf et al., 2005). Although similarly associated with dominant hydrometeors, the initiations in the right and rear anvils had greater heights (>10 km) than those in the forward anvil (<9 km). The relatively low height of the initiations in the forward anvil is attributed to the descent of the particles during their advection from the origin. Therefore, a lifting mechanism should be responsible for the higher flash initiations in the right and rear anvils.

In Fig. 15, the Doppler velocity fields at 6.4° tilt (Fig. 15a) and 15.6° tilt (Fig. 15b) are exhibited. Considering the moving direction of the cluster, a convergence zone identified by the velocity difference could be roughly deduced in the regions circled by the green solid line in Fig. 15a (the height corresponding to the Doppler velocity field was between approximately 5 and 6 km). Divergence could be inferred at 15.6° tilt (Fig. 15b) in a similar position (between approximately 11 and 14 km heights). In fact, the convergence near the southern edge of the main body of the southern supercell could be distinctly inferred at tilts from 3.1° to 12.5° (not shown); thus, rising motion might exist near the southern edge of the 30-dBZ contour. This rising motion lifted the small particles (transported by a size-sorting mechanism) and contributed to the higher position of the particles and flash initiations in the right anvil. Speculatively, the narrow area with weak flash initiations that divides the active initiations near the region overlying the Z_{DR} arc and right anvil might be associated with this rising motion, but further evidence is not available.

Meanwhile, another convergence zone was located at the rear of the updraft (circled by the blue solid lines in Fig. 15). This region had a height of approximately 4 km in Fig. 15a and 9 km in Fig. 15b. The convergence, which should cause a rising motion and initiate high-level flashes in the rear anvil, might have resulted from the interaction between the environmental wind and the upwind outflow from the updraft.

Furthermore, the density distribution of the initial points differed from that of the sources. Fig. 16 shows the relative source density during the four scans. Flashes preferentially propagated through the regions that contained more net charge (Williams et al., 1985; Coleman et al., 2003, 2008). Therefore, the distribution of sources might be related to that of the charge. According to Fig. 5a, the source density mainly represents the distribution of charges at the middle levels. In Fig. 16, the regions at the front of the main updraft of the south supercell contained the most charge (within the south supercell) in all the four stages, which should be attributed to the frequent collision between particles and the strong charging process in the entrainment regions. The region overlying the Z_{DR} arc was also characterized by the second largest source density, primarily because particles carrying charges were transported by the size-sorting mechanism responsible for the Z_{DR} arc. The right anvil had a small source density, although it was still larger than that in the adjacent forward anvil. In contrast, frequent flash initiations were observed in the right anvil, followed by the regions overlying the Z_{DR} arc, adjacent forward anvil and interior and main updraft area. However, the sizes of the flashes initiated in the aforementioned locations were decreased from large to small as follows: the adjacent forward anvil, the region approximately overlying the Z_{DR} arc, the

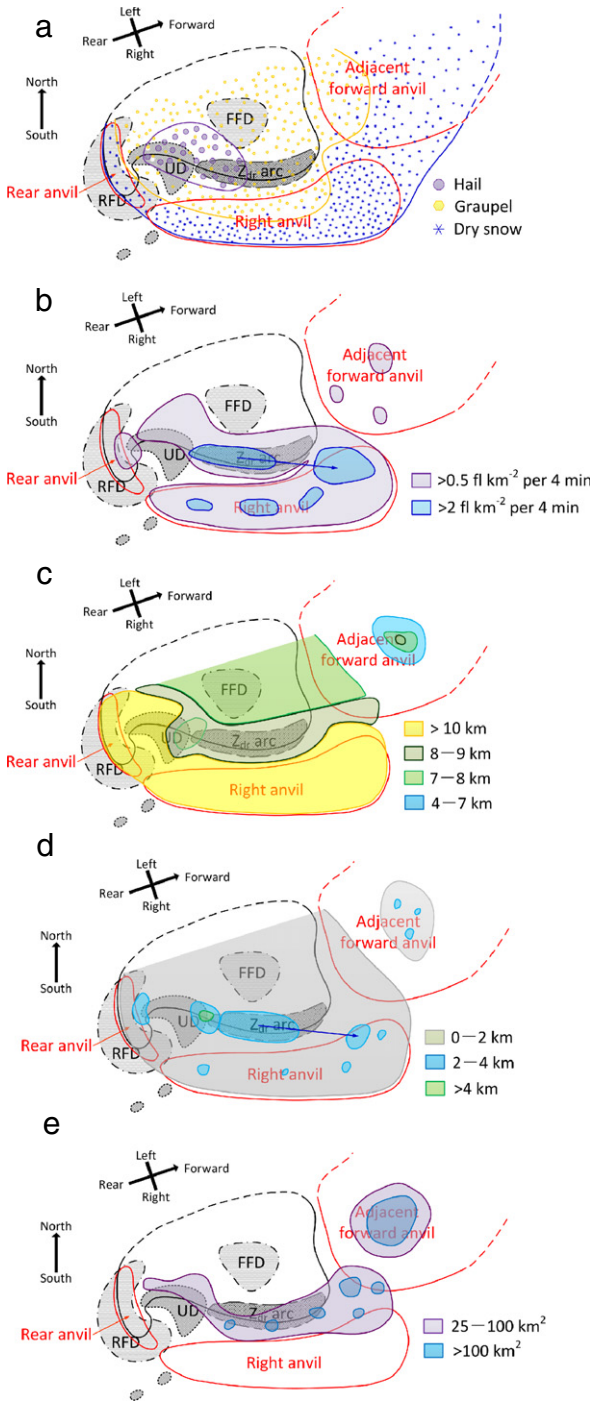

Fig. 14. Schematics of conceptual models that describe the characteristics of flash initiations and their relations to the structures of supercells. (a) The flash initiations and their associated dominant hydrometeors, (b) density of flash initiations, (c) average height of the initial positions of the flashes, (d) height range of the flash initiations, and (e) average area of the convex hull of the flashes at their initial positions.

region around the updraft, and the right and rear anvils. The distribution of the average flash size is further supported by Fig. 17, in which the average areas of the convex hulls of the flashes are shown. The flashes in the rear and right anvils were smallest. The sizes of the flashes increased toward the main body and the forward anvil of the southern supercell. Overall, the largest flashes were more easily identified in the forward anvil. The basic distribution characteristics of the flash size are similar to those exposed by Bruning and MacGorman (2013).

Small flashes and their frequent initiation might be explained by the concept of charge pockets (e.g., Bruning and MacGorman, 2013; Calhoun et al., 2013). In the analysis of a high-precipitation supercell storm, Calhoun et al. (2013) reported that flashes were frequently initiated near the core but were shorter in duration and smaller in horizontal extent relative to flashes far from the updraft. The authors suggested that the small pockets of charge near the core, i.e., opposite polarities in close proximity, could produce a strong electric field in many small regions and frequently initiate flashes. Lightning leaders of each polarity could only propagate a relatively short distance before reaching regions with unfavorable electric potential, leading to small flashes. The results presented here support this view when comparing the sizes and initiations of flashes around the updraft and near the region overlying the Z_{DR} arc. In addition, when we comprehensively consider the source density, flash initiations and flash sizes, the pockets of charge should be more abundant and compact in the right anvil due to the frequent flash initiations, small flashes, and small height interval (i.e., the flashes were initiated in thin layers). Thus, the pockets in the regions around and at the front of the updraft and the regions overlying the Z_{DR} arc, although dominated by charge pockets because of the relatively small flashes, were not as compact as those in the right anvil due to the thicker layer of flash initiations (Fig. 12) and the analogous and smaller initiation density of flashes compared with the right anvil. The rear anvil should also contain charge pockets due to the small flashes. The forward anvil, which usually features large-scale and horizontally extending charges due to advection, tended to yield large flashes. Additionally, the charge pockets tended to occur in regions with wind shear. The right anvil and the region overlying the Z_{DR} arc were associated with convergence along the southern edge of the main body of the southern supercell; the rear anvil was associated with convergence upwind of the updraft, and the region around the updraft was associated with large horizontal shear (Klemp and Wilhelmson, 1978).

6. Conclusion

In this study, we examined a cluster of supercells on 10–11 May 2010 that produced frequent tornadoes, hail, strong wind, extremely active in-cloud flashes, a low proportion of CG flashes (1.07%), and a high proportion of PCG flashes (56.70%) with a generally inverted charge structure.

Flash initiations in areas dominated by graupel, dry snow, small hail and crystals accounted for 44.3%, 44.1%, 8.0% and 3.0% of the total available samples, respectively. The maximum number of flash initiations occurred at 7 km for graupel and 11 km for dry snow.

In the tornadic stage examined in this paper, the flash initiations in areas dominated by graupel mainly occupied the main body, right flank, and forward flank of the supercells, while the flashes that corresponded to dry snow were located at the outskirts of the adjacent forward anvil, right anvil, and rear anvil. The flash initiations associated with small hail were located around the main updraft and inclined toward the front.

A large number of flash initiations with values larger than 2 fl km^{-2} per 4 min usually occurred in the region overlying the Z_{DR} arc (particularly during the early periods of tornadic-stage supercells) and the right anvil, which were divided by a narrow area with a density smaller than 0.5 fl km^{-2} per 4 min. The updraft, rear of the supercell, FFD and adjacent forward anvil essentially yielded less flash initiations. The density of flash initiations was not consistent with that of the flash sources, whose large density distinctly occupied the front of the updraft and the region overlying the Z_{DR} arc.

The average initial height of the flashes decreased from the rear to the front and from right to left of the storms. The right and rear anvils and the region west of the updraft were characterized by an average initial height larger than 10 km, while that of the region to the front of the updraft was 7–8 km; the region overlying the Z_{DR} arc and its forward extensions were 8–9 km. The adjacent forward region, although

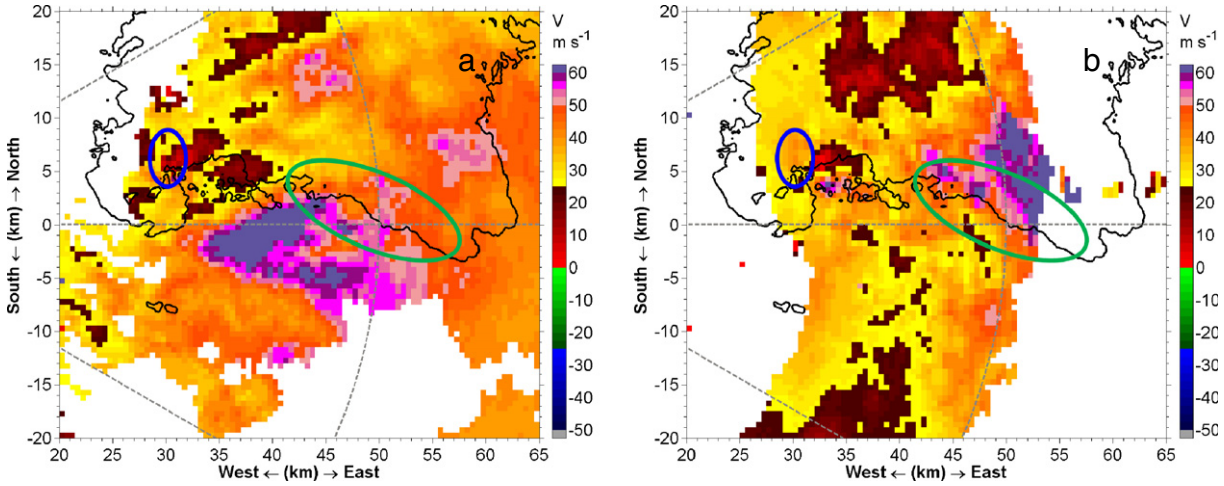

Fig. 15. Doppler velocities at 6.4° tilt (a) and 15.6° tilt (b) superposed by the 30-dBZ contour at 0.9° tilt at 2250:14 UTC. The green ellipses roughly circle the region with convergence in (a) and divergence in (b). The blue ellipses roughly circle the region with convergence in (a) and (b).

interspersed by a few flash initiations with relative large heights, had a lower average height of flash initiations overall.

The height range over which flashes were initiated was maximized at the front of the updraft, where the range was larger than 4 km. A height range between 2 km and 4 km was found in the region overlying the Z_{DR} arc during the early period of the tornadic-stage supercell and the eastern part of the right anvil during the vigorous period of the tornadic-stage supercell. Generally, the flash initiations in the right, rear and adjacent forward anvils had small height ranges (<2 km), with values only surpassing 2 km at the local scale.

The flashes that initiated in the adjacent forward anvils were generally the largest, featuring an average convex-hull area larger than 100 km^2. The average area of the convex hull of the flashes that were initiated in the regions ahead of the main updraft and approximately overlying the Z_{DR} arc ranged 25–100 km^2 overall; locally, the values were larger than 100 km^2. Flashes that were initiated in the rear and

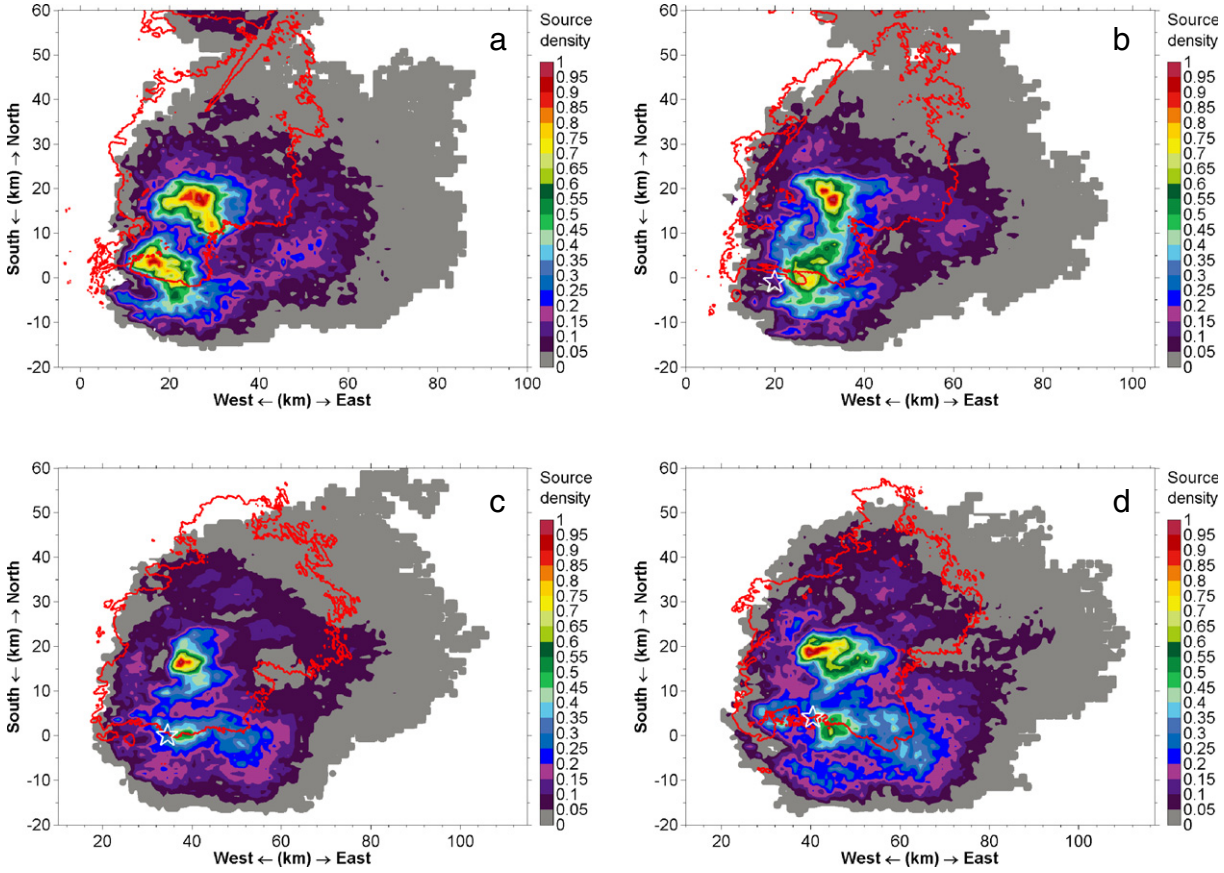

Fig. 16. Relative source density superposed by the 30-dBZ contour at 0.9° tilt. (a) 2234:09 UTC; (b) 2238:27 UTC; (c) 2245:56 UTC; and (d) 2250:14 UTC. The statistical grids are 1 km × 1 km. The data are shown after bilinear interpolation for better display. The same as in Fig. 17.

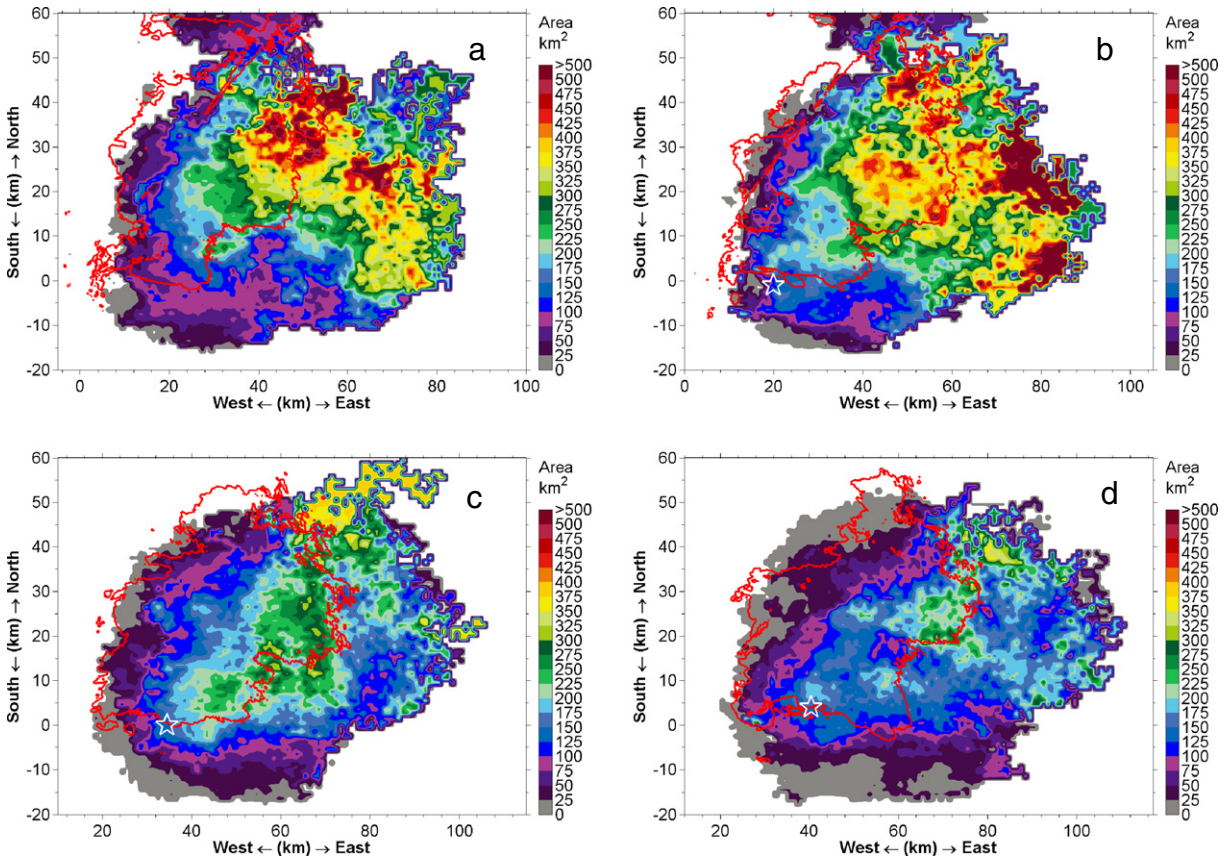

Fig. 17. Average area of the convex hull of the flashes superposed by the 30-dBZ contour at 0.9° tilt. (a) 2234:09 UTC; (b) 2238:27 UTC; (c) 2245:56 UTC; and (d) 2250:14 UTC. The values that show large gradients along the edges between the grids with values and those without values are not reliable due to the bilinear interpolation which helps to show the images better.

right anvils were the smallest, with convex-hull areas under 25 km^2. The average convex-hull area of the flashes for the entire supercell distinctly increased from the rear to the front and from the south to the main body of the supercell.

This study supports the concept of charge pockets (e.g., Bruning and MacGorman, 2013; Calhoun et al., 2013) and further deduces that the charge pockets should be more abundant and compact in the right anvil than in the region around the front of the updraft and the region overlying the Z_{DR} arc. Charge pockets tend to exist in regions with wind shear.

Acknowledgments

The author is particularly grateful to Pengfei Zhang for his important assistance in radar data processing. My thanks also go to Matthew Elliott and Erica Griffin, who helped to collect, examine, and interpret the dataset. The author is grateful to the Cooperative Institute for Mesoscale Meteorological Studies and NOAA/OAR/National Severe Storms Laboratory which provided the necessary conditions to promote the author's research work and cooperation and communication.

This research was supported by the 973 Program (2014CB441402, 2014CB441406), the Basic Research Fund of Chinese Academy of Meteorological Sciences (2013Z006, 2014R017), and the Natural Science Foundation of China (41005006).

References

Balakrishnan, N., Zrnić, D.S., 1990. Use of polarization to characterize precipitation and discriminate large hail. J. Atmos. Sci. 47, 1525–1540.
Berdeklis, P., List, R., 2001. The ice crystal–graupel collision charging mechanism of thunderstorm electrification. J. Atmos. Sci. 58, 2751–2770.
Branick, M.L., Doswell III, C.A., 1992. An observation of the relationship between supercell structure and lightning ground strike polarity. Weather Forecast. 7, 13–149.
Browning, K.A., Foote, G.B., 1976. Airflow and hail growth in supercell storms and some implications for hail suppression. Q. J. R. Meteorol. Soc. 102, 499–533.
Bruning, E.C., MacGorman, D.R., 2013. Theory and observations of controls on lightning flash size spectra. J. Atmos. Sci. 70, 4012–4028.
Bruning, E.C., Rust, W.D., Schuur, T.J., MacGorman, D.R., Krehbiel, P.R., Rison, W., 2007. Electrical and polarimetric radar observations of a multicell storm in TELEX. Mon. Weather Rev. 135, 2525–2544.
Bruning, E.C., Rust, W.D., MacGorman, D.R., Biggerstaff, M.I., Schuur, T.J., 2010. Formation of charge structures in a supercell. Mon. Weather Rev. 138, 3740–3761.
Bruning, E.C., Weiss, S.A., Calhoun, K.M., 2014. Continuous variability in thunderstorm primary electrification and an evaluation of inverted-polarity terminology. Atmos. Res. 135–136, 274–284.
Calhoun, K.M., MacGorman, D.R., Ziegler, C.L., Biggerstaff, M.I., 2013. Evolution of lightning activity and storm charge relative to dual-doppler analysis of a high-precipitation supercell storm. Mon. Weather Rev. 141, 2199–2223.
Coleman, L.M., Marshall, T.C., Stolzenburg, M., Hamlin, T., Krehbiel, P.R., Rison, W., Thomas, R.J., 2003. Effects of charge and electrostatic potential on lightning propagation. J. Geophys. Res. 108, 4298. http://dx.doi.org/10.1029/2002JD002718.
Coleman, L.M., Stolzenburg, M., Marshall, T.C., Stanley, M., 2008. Horizontal lightning propagation, preliminary breakdown, and electric potential in New Mexico thunderstorms. J. Geophys. Res. 113, D09208. http://dx.doi.org/10.1029/2007JD009459.
Cummins, K.L., Murphy, M.J., Bardo, E.A., Hiscox, W.L., Pyle, R.B., Pifer, A.E., 1998. A combined TOA/MDF technology upgrade of the U.S. National Lightning Detection Network. J. Geophys. Res. 103 (D8), 9035–9044.
Davies-Jones, R., 2015. A review of supercell and tornado dynamics. Atmos. Res. 158–159, 274–291.
Dawson II, D.T., Mansell, E.R., Jung, Y., Wicker, L.J., Kumjian, M.R., Xue, M., 2014. Low-level Z_{DR} signatures in supercell forward flanks: the role of size sorting and melting of hail. J. Atmos. Sci. 71, 276–299.
Dotzek, N., Holler, H., Thery, C., Fehr, T., 2001. Lightning evolution related to radar-derived microphysics in the 21 July 1998 EULINOX supercell storm. Atmos. Res. 56, 335–354.
Dwyer, J.R., Uman, M.A., 2014. The physics of lightning. Phys. Rep. 534, 147–241.
Goodman, S.J., Coauthors, 2005. The North Alabama lightning mapping array: recent severe storm observations and future prospects. Atmos. Res. 76, 423–437.
Johnson, E.V., Mansell, E.R., 2006. Three-dimensional lightning mapping of the Central Oklahoma supercell on 26 May 2004. Extended Abstracts, Second Conf.

on Meteorological Applications of Lightning Data, Atlanta, GA, Amer. Meteor. Soc., 6.5.
Klemp, J.B., Wilhelmson, R.B., 1978. The simulation of threedimensional convective storm dynamics. J. Atmos. Sci. 35, 1070–1096.
Knupp, K.R., Peach, S., Goodman, S., 2003. Variations in cloud-to-ground lightning characteristics among three adjacent tornadic supercell storms over the Tennessee valley region. Mon. Weather Rev. 131, 172–188.
Krehbiel, P.R., Thomas, R.J., Rison, W., Hamlin, T., Harlin, J., Davis, M., 2000. GPS-based mapping system reveals lightning inside storms. EOS Trans. Am. Geophys. Union 81 (3), 21–25.
Kuhlman, K.M., MacGorman, D.R., Biggerstaff, M.I., Krehbiel, P.R., 2009. Lightning initiation in the anvils of two supercell storms. Geophys. Res. Lett. 36, L07802. http://dx.doi.org/10.1029/2008GL036650.
Kumjian, M.R., 2013a. Principles and applications of dual-polarization weather radar. Part I: description of the polarimetric radar variables. J. Oper. Meteorol. 1 (19), 226–242.
Kumjian, M.R., 2013b. Principles and applications of dual-polarization weather radar. Part II: warm- and cold-season applications. J. Oper. Meteorol. 1 (19), 243–264.
Kumjian, M.R., 2013c. Principles and applications of dual-polarization weather radar. Part III: artifacts. J. Oper. Meteorol. 1 (19), 265–274.
Kumjian, M.R., Ryzhkov, A.V., 2008. Polarimetric signatures in supercell thunderstorms. J. Appl. Meteorol. Climatol. 47, 1940–1961.
Kumjian, M.R., Ryzhkov, A.V., 2009. Storm-relative helicity revealed from polarimetric radar measurements. J. Atmos. Sci. 66, 667–685.
Lang, T.J., Rutledge, S.A., Dye, J.E., Venticinque, M., Laroche, P., Defer, E., 2000. Anomalously low negative cloud-to-ground lightning flash rates in intense convective storms observed during STERAO-A. Mon. Weather Rev. 128, 160–173.
Lemon, L.R., Doswell III, C.A., 1979. Severe thunderstorm evolution and mesocyclone structure as related to tornadogenesis. Mon. Weather Rev. 107, 1184–1197.
Li, Y., Zhang, G., Wen, J., Wang, D., Wang, Y., Zhang, T., Fan, X., Wu, B., 2013. Electrical structure of a Qinghai–Tibet Plateau thunderstorm based on three-dimensional lightning mapping. Atmos. Res. 134, 137–149.
Loney, M.L., Zrnić, D.S., Straka, J.M., Ryzhkov, A.V., 2002. Enhanced polarimetric radar signatures above the melting level in a supercell storm. J. Appl. Meteorol. 41, 1179–1194.
Lund, N.R., MacGorman, D.R., Schuur, T.J., Biggerstaff, M.I., 2009. Relationships between lightning location and polarimetric radar signatures in a small mesoscale convective system. Mon. Weather Rev. 137, 4151–4170.
MacGorman, D.R., Coauthors, 2008. TELEX The Thunderstorm Electrification and Lightning Experiment. Bull. Am. Meteorol. Soc. 89, 997–1013.
MacGorman, D.R., Burgess, D.W., Mazur, V., Rust, W.D., Taylor, W.L., Johnson, B.C., 1989. Lightning rates relative to tornadic storm evolution on 22 May 1981. J. Atmos. Sci. 46, 221–250.
MacGorman, D.R., Rust, W.D., Krehbiel, P.R., Rison, W., Bruning, E.C., Wiens, K.C., 2005. The electrical structure of two supercell storms during STEPS. Mon. Weather Rev. 133, 2583–2607.
Manzato, A., Davolio, S., Miglietta, M.M., Pucillo, A., Setvak, M., 2015. 12 September 2012: a supercell outbreak in NE Italy? Atmos. Res. 153, 98–118.
Markowski, P.M., 2008. A comparison of the midlevel kinematic characteristics of a pair of supercell thunderstorms observed by airborne Doppler radar. Atmos. Res. 88, 314–322.
Mazur, V., 1989a. Triggered lightning strikes to aircraft and natural intracloud discharges. J. Geophys. Res. 94, 3311–3325.
Mazur, V., 1989b. Physical model of lightning initiation on aircraft in thunderstorms. J. Geophys. Res. 94, 3326–3340.
Nelson, S.P., 1983. The influence of storm flow structure on hail growth. J. Atmos. Sci. 40, 1965–1983.
Orville, R.E., 2008. Development of National Lightning Detection Network. Bull. Am. Meteorol. Soc. 89, 180–190.
Orville, R.E., Huffines, G.R., 2001. Cloud-to-ground lightning in the United States: NLDN result in the first decade, 1989–98. Mon. Weather Rev. 129, 1179–1193.
Palmer, R.D., Bodine, D., Kumjian, M., Cheong, B., Zhang, G., Cao, Q., Bluestein, H.B., Ryzhkov, A., Yu, T.-Y., Wang, Y., 2011. Observations of the 10 May 2010 tornado outbreak using OU-Prime: potential for new science with high-resolution polarimetric radar. Bull. Am. Meteorol. Soc. 92, 871–891.
Park, H., Ryzhkov, A.V., Zrnic, D.S., Kim, K.-E., 2009. The hydrometeor classification algorithm for the polarimetric WSR-88D: description and application to an MCS. Weather Forecast. 24, 730–748.
Payne, C.D., Schuur, T.J., MacGorman, D.R., Biggerstaff, M.I., Kuhlman, K.M., Rust, W.D., 2010. Polarimetric and electrical characteristics of a lightning ring in a supercell storm. Mon. Weather Rev. 138, 2405–2425.
Proctor, D.E., 1991. Regions where lightning flashes began. J. Geophys. Res. 96, 5099–5112.
Rison, W., Thomas, R.J., Krehbiel, P.R., Hamlin, T., Harlin, J., 1999. A GPS-based three-dimensional lightning mapping system: initial observations in central New Mexico. Geophys. Res. Lett. 26, 3573–3576.
Rust, W.D., Coauthors, 2005. Inverted-polarity electrical structures in thunderstorms in the Severe Thunderstorm Electrification and Precipitation Study. Atmos. Res. 76, 247–271.
Ryzhkov, A.V., Kumjian, M.R., Ganson, S.M., Khain, A.P., 2013. Polarimetric radar characteristics of melting hail. Part I: theoretical simulations using spectral microphysical modeling. J. Appl. Meteorol. Climatol. 52, 2849–2870.
Saunders, C.P.R., Peck, S.L., 1998. Laboratory studies of the influence of the rime accretion rate on charge transfer during crystal/graupel collisions. J. Geophys. Res. 103 (D12), 13949–13956.
Saunders, C.P.R., Bax-Norman, H., Emerisic, C., Avila, E.E., Castellano, N.E., 2006. Laboratory studies of the effect of cloud conditions on graupel/crystal charge transfer in thunderstorm electrification. Q. J. R. Meteorol. Soc. 132, 2653–2673.
Shao, X.M., Krehbiel, P.R., 1996. The spatial and temporal development of intracloud lightning. J. Geophys. Res. 101, 641–668.
Snyder, J.C., Bluestein, H.B., Zhang, G., Frasier, S.J., 2010. Attenuation correction and hydrometeor classification of high-resolution, x-band, dual-polarized mobile radar measurements in severe convective storms. J. Atmos. Ocean. Technol. 27, 1979–2001.
Snyder, J.C., Bluestein, H.B., Vekatesh, V., Frasier, S.J., 2013. Observations of polarimetric signatures in supercells by an x-band mobile Doppler radar. Mon. Weather Rev. 141, 3–29.
Soula, S., Seity, Y., Feral, L., Sauvageot, H., 2004. Cloud-to-ground lightning activity in hail-bearing storms. J. Geophys. Res. 109, D02101. http://dx.doi.org/10.1029/2003JD003669.
Stolzenburg, M., Rust, W.D., Marshall, T.C., 1998. Electrical structure in thunderstorm convective regions 3. Synthesis. J. Geophys. Res. 103 (D12), 14097–14108.
Straka, J.M., Zrnić, D.S., Ryzhkov, A.V., 2000. Bulk hydrometeor classification and quantification using polarimetric radar data: synthesis of relations. J. Appl. Meteorol. 39, 1341–1372.
Takahashi, T., 1978. Riming electrication as a charge generation mechanism in thunderstorm. J. Atmos. Sci. 35, 1536–1548.
Tessendorf, S.A., Miller, L.J., Wiens, K.C., Rutledge, S.A., 2005. The 29 June 2000 supercell observed during STEPS. Part I: kinematics and microphysics. J. Atmos. Sci. 62, 4127–4150.
Tessendorf, S.A., Wiens, K.C., Rutledge, S.A., 2007. Radar and lightning observations of the 3 June 2000 electrically inverted storm from STEPS. Mon. Weather Rev. 135, 3665–3681.
Thomas, R.J., Krehbiel, P.R., Rison, W., Hamlin, T., Harlin, J., Shown, D., 2001. Observations of VHF source powers radiated by lightning. Geophys. Res. Lett. 28, 143–146.
Thomas, R., Krehbiel, P., Rison, W., Hunyady, S., Winn, W., Hamlin, T., Harlin, J., 2004. Accuracy of the lightning mapping array. J. Geophys. Res. 109, D14207. http://dx.doi.org/10.1029/2004JD004549.
Van Den Broeke, M.S., Straka, J.M., Rasmussen, E.N., 2008. Polarimetric radar observations at low levels during tornado life cycles in a small sample of classic southern plains supercells. J. Appl. Meteorol. Climatol. 47, 1232–1247.
Wang, P.K., Lin, H.-M., Su, S.-H., 2010. The impact of ice microphysical processes on the life span of a midlatitude supercell storm. Atmos. Res. 97, 450–461.
Weiss, S.A., MacGorman, D.R., Calhoun, K.M., 2012. Lightning in the anvils of supercell thunderstorms. Mon. Weather Rev. 140, 2064–2079.
Wiens, K.C., Rutledge, S.A., Tessendorf, S.A., 2005. The 29 June 2000 supercell observed during STEPS. Part II: lightning and charge structure. J. Atmos. Sci. 62, 4151–4177.
Williams, E.R., Cooke, C.M., Wright, K.A., 1985. Electrical discharge propagation in and around space charge clouds. J. Geophys. Res. 90, 6059–6070.